

Article

Using Machine Learning to Extract Building Inventory Information Based on LiDAR Data

Gordana Kaplan ^{1,*} , Resul Comert ¹, Onur Kaplan ² , Dilek Kucuk Matci ¹  and Ugur Avdan ¹ 

¹ Institute of Earth and Space Sciences, Eskisehir Technical University, Eskisehir 26555, Turkey

² College of Engineering and Technology, American University of the Middle East, Egaila 54200, Kuwait

* Correspondence: kaplangorde@gmail.com; Tel.: +90-536-697-5605

Abstract: The extraction of building inventory information is vital for damage assessment and planning and modelling studies. In the last few years, the conventional data extraction for building inventory was overcome using various remote sensing data and techniques. The main objectives of this study were to supply the necessary data for the structural engineers to calculate the seismic performance of existing structures. Thus, we investigated light detection and ranging (LiDAR) derivatives data to classify buildings and extract building inventory information, such as different heights of the buildings and footprint area. The most important data to achieve this was also investigated and classified using machine learning methods, such as Random Forest, Random Tree, and Optimized Forest, over the object-based segmentation results. All of the machine learning methods successfully classified the buildings with high accuracy, whereas the other methods outperformed RT. The height and footprint area results show that the archived sensitivity of the building inventory information is sufficient for the data to be further used in different applications, such as detailed structural health monitoring. Overall, this study presents a methodology that can accurately extract building information. In light of the results, future studies can be directed for investigations on determining the construction year using remote sensing data, such as multi-temporal satellite imagery.

Keywords: remote sensing; LiDAR; building; height; machine learning; random forest; random tree; optimized tree



Citation: Kaplan, G.; Comert, R.; Kaplan, O.; Matci, D.K.; Avdan, U. Using Machine Learning to Extract Building Inventory Information Based on LiDAR Data. *ISPRS Int. J. Geo-Inf.* **2022**, *11*, 517. <https://doi.org/10.3390/ijgi11100517>

Academic Editors: Maria Antonia Brovelli and Wolfgang Kainz

Received: 1 September 2022

Accepted: 4 October 2022

Published: 15 October 2022

Publisher's Note: MDPI stays neutral with regard to jurisdictional claims in published maps and institutional affiliations.



Copyright: © 2022 by the authors. Licensee MDPI, Basel, Switzerland. This article is an open access article distributed under the terms and conditions of the Creative Commons Attribution (CC BY) license (<https://creativecommons.org/licenses/by/4.0/>).

1. Introduction

In earthquake-prone areas, it is critical to assess the seismic performance of existing structures to estimate potential damages from a future earthquake. Many approaches with varying levels of detail have been devised to determine or estimate the seismic susceptibility of existing structures. These approaches include street screening, more comprehensive preliminary evaluation, and code-based assessment [1]. In all three groups' methodologies, there are similar key parameters. Experts determine these facts on-site in the traditional approach. These traditional investigations are challenging, depending on the number of structures to be investigated.

Determining a building's fundamental vibration period is critical for earthquake design and seismic hazard assessment. The construction period is determined by the mass and rigidity of the structure. It may be calculated using eigenvalue or pushover analysis on a numerical model of the building. However, when performing seismic vulnerability assessment studies on an urban scale, the seismic performance of hundreds or thousands of structures must be estimated [2]. Therefore, using computer analysis to calculate the vibration period of each structure in the studied urban area is not practicable. As a result, simple models may be used to determine the building period in relation to the building height [3]. Traditional field survey methods might take a long time to measure the height of each structure in a large building stock. As a result, cutting-edge technology such as remote sensing apps should be employed to assess building height [4].

A building's fundamental vibration period is a vital earthquake engineering metric in earthquake-resistant design and seismic performance assessment. Most static design approaches use a design spectrum to calculate the corresponding seismic lateral force. As a result, the earthquake power is a function of the building's fundamental vibration period [5,6]. The basic period can be computed based on modelling or simplified empirical relationships in seismic design codes. Empirical equations are preferred for rapid assessment applications [7].

A building inventory based on remote sensing may be collected using a variety of data formats. It is possible to obtain critical risk assessment building factors such as construction year, building height, and building area. At the same time, human resources may be directed toward risk assessment, analysis, and result interpretation. These data may be used and evaluated by automatic machine learning algorithms for quick and advanced risk assessment and other seismic vulnerability assessment research.

Automatic and semi-automatic building extraction and determination of building height are essential for urban planning, 3D city modelling, urban monitoring, pre-disaster building risk assessment, disaster management, and other geospatial applications [8–10]. In the last few years, remote sensing data such as aerial, optical satellite, and light detection and ranging (LiDAR) have been proven to be efficient for building extraction and height determination [8,9,11]. Edge/line extraction [12], morphological operators [13] and object-based image analysis (OBIA) [14] approaches have been used in image-based building extraction. In determining the building height with image-based methods, shadow-based methods [9,15] and height determination approaches from a digital surface model (DSM) produced from image pairs have been applied [16]. Although image-based methods are successful in building extraction, the complex structure of urban areas, the presence of vegetation and the shadow problem reduce the success of the methods in determining the building height [17].

Building extraction is performed directly from the LiDAR point cloud for 3D building reconstruction. In this approach, planar building roofs are extracted using Hough transform and Random Sample Consensus (RANSAC) [18–22] and Region Growing [23,24], or rule-based segmentation [19] methods by using the geometric properties of the points. Although these methods, which extract buildings directly from the extensive point cloud, are manageable in terms of applicability, they have changes such as extracting non-building planar objects as building roofs and the inability to extract curve building roofs [25,26].

Using satellite or aerial images and LiDAR data by fusion in 2D building extraction studies for disaster management or other geospatial applications is very common. Eliminating the ground feature from the LiDAR data and filtering the vegetation from the spectral bands of the image increases the accuracy of building extraction [27,28]. OBIA is the preferred approach in optical images and LiDAR fusion studies for building extraction due to the combined use of geometric, spectral, and topographic features [29–32].

Although fusion datasets give successful results, having both LiDAR and optics image datasets belonging to a field is not always possible. There are studies in which 2D building footprints extraction is done only on LiDAR derivatives. In these studies, buildings extracted with LiDAR-derived DSM threshold value yielded better results than image-based DSM data [33], and building footprints were successfully extracted from LiDAR-derived DSM and Digital Terrain Model (DTM) with OBIA rule-based classification [34]. Additionally, based on the LiDAR DSM and DTM data, the building roof footprint extracted and building types were classified with OBIA and RF classifiers [35]. The relevance of that kind of data in building extraction, the usability of the derived building footprints, and the heights in assessing the seismic hazards of structures have not been studied, despite prior work on building extraction using LiDAR derivatives [30,34].

Thus, this study's main objectives have been to supply the data that can be obtained remotely for structural engineers to make primary calculations for the seismic performance of existing structures. Thus, we use six steps for using different raster LiDAR derivatives, and achieving the goal of the paper; (i) OBIA segmentation for building extraction; (ii) ex-

ploring the most essential parameters for building extraction; (iii) investigating different machine learning methods for building extraction; (iv) exploring different data split for better building classification; (v) estimating building heights; and (vi) estimating building footprint area.

The paper has been structured in five parts; after the introduction follows the material and methods part, where details about the study area, the data, and the used methods have been given. The methodology is constructed of different parts; remote sensing data preparation, where the image segmentation and the preparation of the data have been explained; machine learning classification and accuracy assessment; and building extraction and height and footprint area calculation. Further along, the results were presented, supported with a discussion and the conclusion.

2. Materials and Methods

2.1. Study Area

The study area (300 ha) is comprised of an urban area with a total of 312 buildings in the west part of the city of Skopje, the capital of North Macedonia (Figure 1). The study area is divided into two parts, with the Vardar river with a width of approximately 60 m. The left part of the study area contains dense and low residential grid-like buildings with a maximum of 10 m height, while on the right side, there are higher residential and commercial buildings with a maximum height of 70 m. The study area is generally flat, and the surface elevation of the study area varies from 250–327, while the terrain elevation is from 250–325. Besides buildings, the study area contains many trees, three bridges, and a riverbank of 20 m in width from both sides.

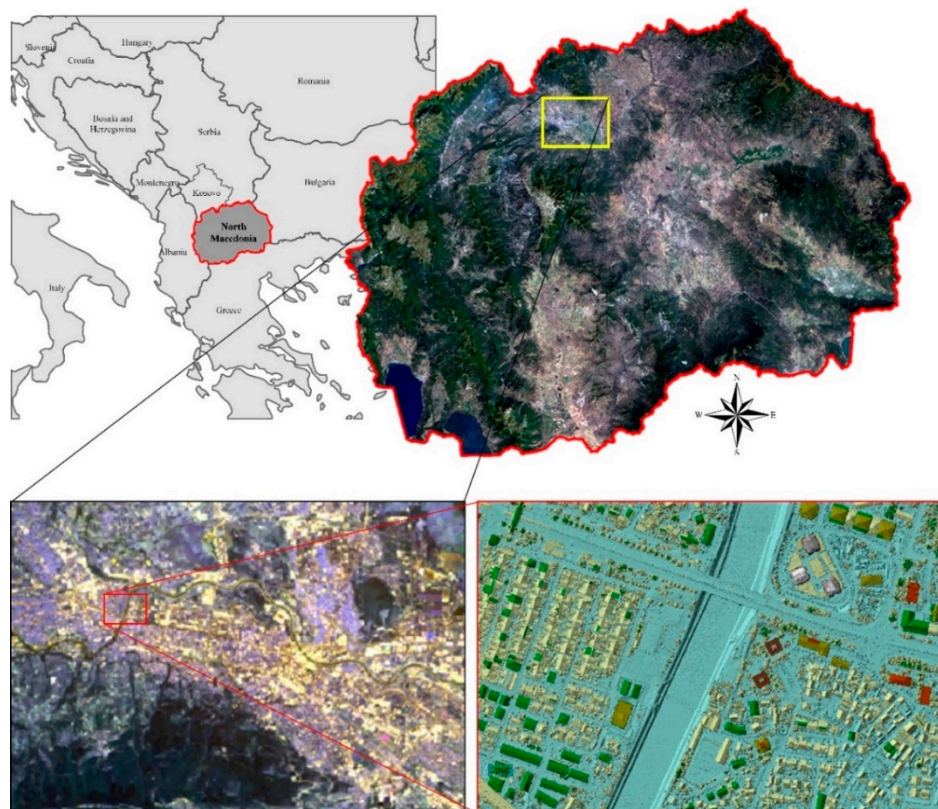


Figure 1. Study area.

The study area is located in a high-risk seismic region with a history of devastating earthquakes. Thus, a shallow, magnitude 6.1 earthquake with an intensity rating of IX (Mercalli scale) struck the city in 1963, where the catastrophe resulted in significant loss of life and property. Over 1000 people were killed, 4000 injured, and over 200,000 displaced.

Almost 80% of the city was destroyed, and many public buildings, schools, hospitals, and historical sites were severely damaged. In more recent times, in 2016, a strong, magnitude ML5.3 earthquake stroke the capital [36].

2.2. Data

In this study, we use LiDAR derivatives for building extraction. Thus, the primary data in this study is LiDAR remote sensing. The LiDAR data were obtained from the Cadastral Agency of North Macedonia. The data acquisition was made with an aerial platform, Cessna 402B, and Riegl VQ-780i sensor system. The data collection was done on 3 May 2019, under a clear sky, and 11 C air temperature. The ground sampling distance of the LiDAR data is 5 points/m² (Figure 2).

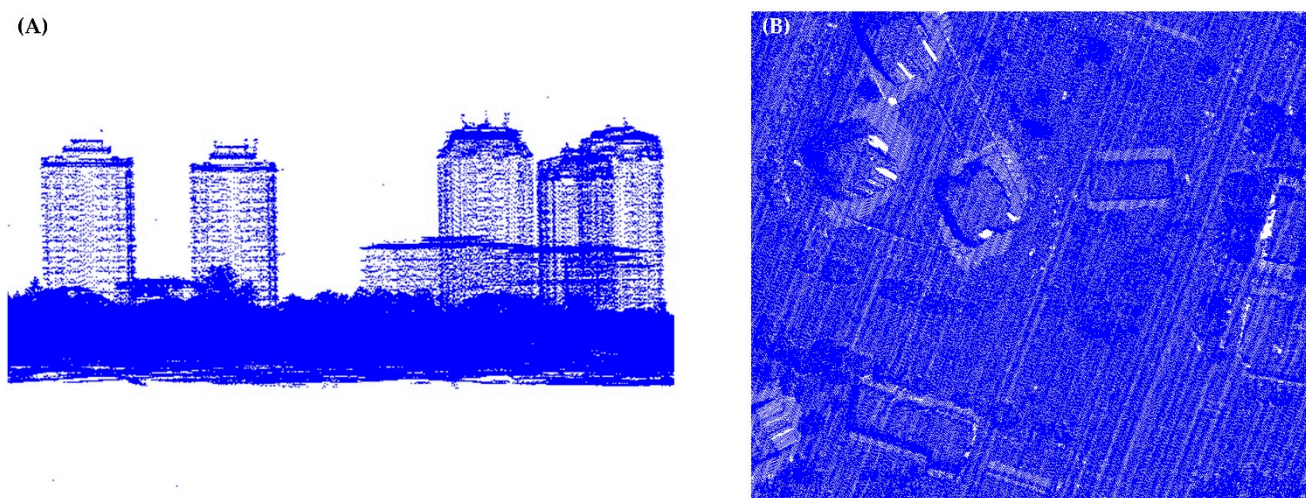


Figure 2. Example of the point cloud used in this study; (A) front view; and (B) top view.

A 30 cm spatial resolution DSM, DTM, intensity, number of return (NOR), and DSM–DTM difference maps produced from a LiDAR point cloud were used to extract building footprints and determine their heights. To produce LiDAR derivatives, firstly, the noise points were eliminated by applying a statistical outlier filter (SOR) to the original point cloud. Using the filtered data, DSM, intensity and NOR maps were generated by linear interpolation. Ground points were extracted by applying a Cloth Simulation Filtering (CSF) algorithm to the point cloud to generate the DTM [37]. CSF parameters were set as topography: flat, cloth resolution: 0.5, maximum iteration: 1000, and classification threshold: 0.1 in extraction of ground points. Examples of the LiDAR derived data are given in Figure 3.

2.3. Methods

The methodology in this study is constructed of three different steps; (i) remote sensing data preparation; (ii) machine learning classification; and (iii) building extraction and height calculation. The methodologies flowchart is given in Figure 4, while the details of each part will be explained in the following sections.

2.3.1. Image Segmentation and Analysis Dataset Preparation

The initial phase in the OBIA process is image segmentation. At this level, the goal is to generate meaningful image objects from the segmented layers. In OBIA, the most used segmentation approach is multi-resolution segmentation (MRS). The segmentation process in this approach begins at the pixel level, and the merging process occurs based on the spatial and spectral heterogeneity of the candidate chosen picture item with surrounding image objects [38]. To construct optimal image objects using the MRS approach, the user must decide the scale, shape, compactness, and layer weights. The scale parameter

determines the size or heterogeneity of the picture objects that will be created. When the scale parameter is set to a big value, large image objects are created and vice-versa. The shape parameter, with values ranging from 0 to 1, is used to calculate the weights of spatial and spectral functions in the merging factor. In the shape function computation, the compactness parameter influences the compactness and smoothness of the generated picture objects. Layer weights indicate the relevance of segmentation layers compared to other layers [39]. To determine the optimal segmentation parameters, we used the trial and error method based on visual analysis [40]. Different combinations of intensity, DSM, DSM–DTM difference, number of returns, and slope layers were tested to generate optimum building objects. The best separation result was obtained with the combination of DSM–DTM difference and DSM. The optimum segmentation parameters for this combination were determined as scale: 25, shape: 0.2, and compactness: 0.5. After the segmentation, the variables used in the classification phase were determined for the created objects. At this stage, the mean values of the input layers, the geometric variables of the objects and the textural variables calculated from the input layers were used. As a result of the visual analysis, it was determined that 25 variables were suitable for classification (Table 1). Afterwards, all of the produced objects were labeled into two classes, namely, buildings and non-buildings. In this stage, we aimed for the roofs to extract the footprint of the buildings (Figure 5). The labelling process was done using high-resolution imagery from Google Earth, an orthophoto with 50 cm spatial resolution, and hillsides. To investigate the effect of the training dataset size on extracting building footprints, the labelled dataset was randomly divided into two different datasets, 70% train, 30% test and 30% train, 70% test, using the R statistical program.

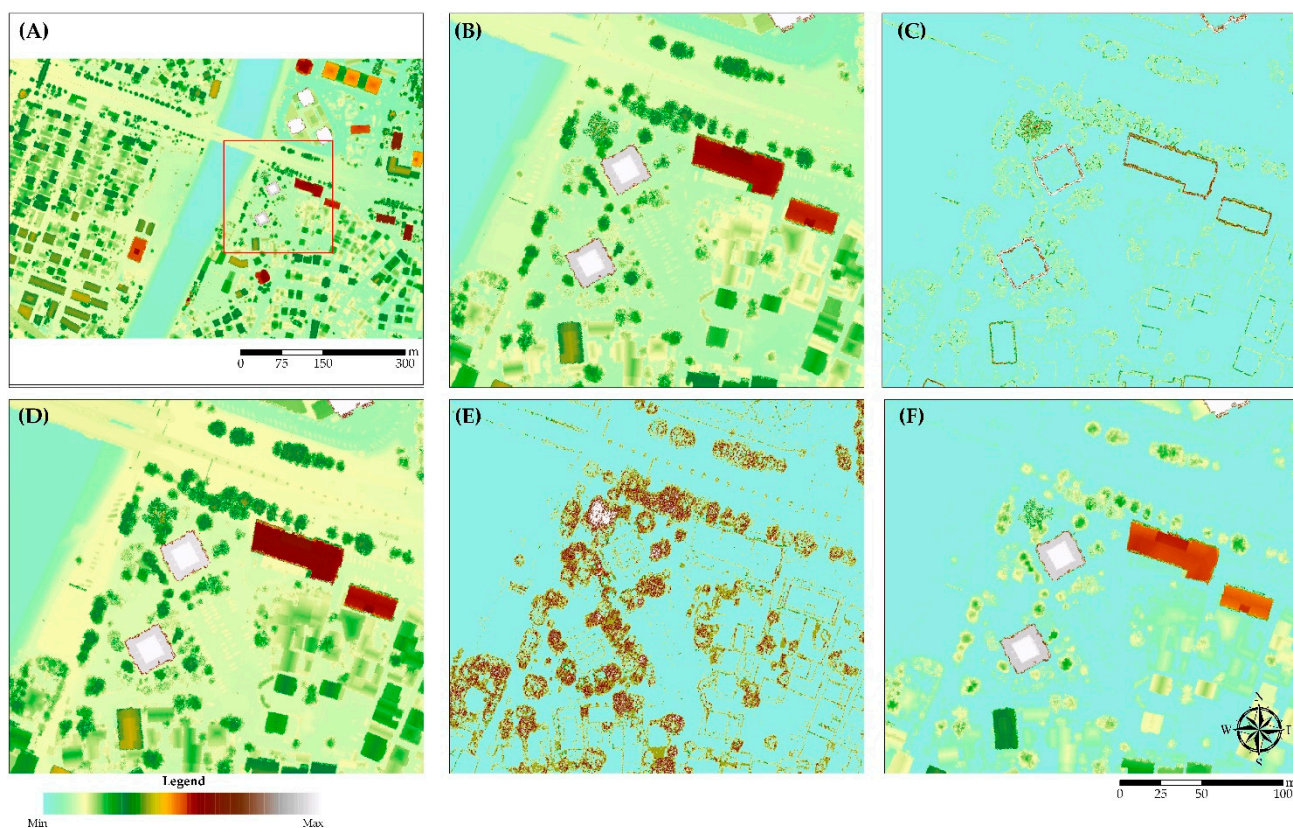


Figure 3. Data samples used in the study; (A) DSM of the study area; (B) DSM detail; (C) DSM slope detail; (D) intensity; (E) number of return; (F) and DSM–DTM difference.

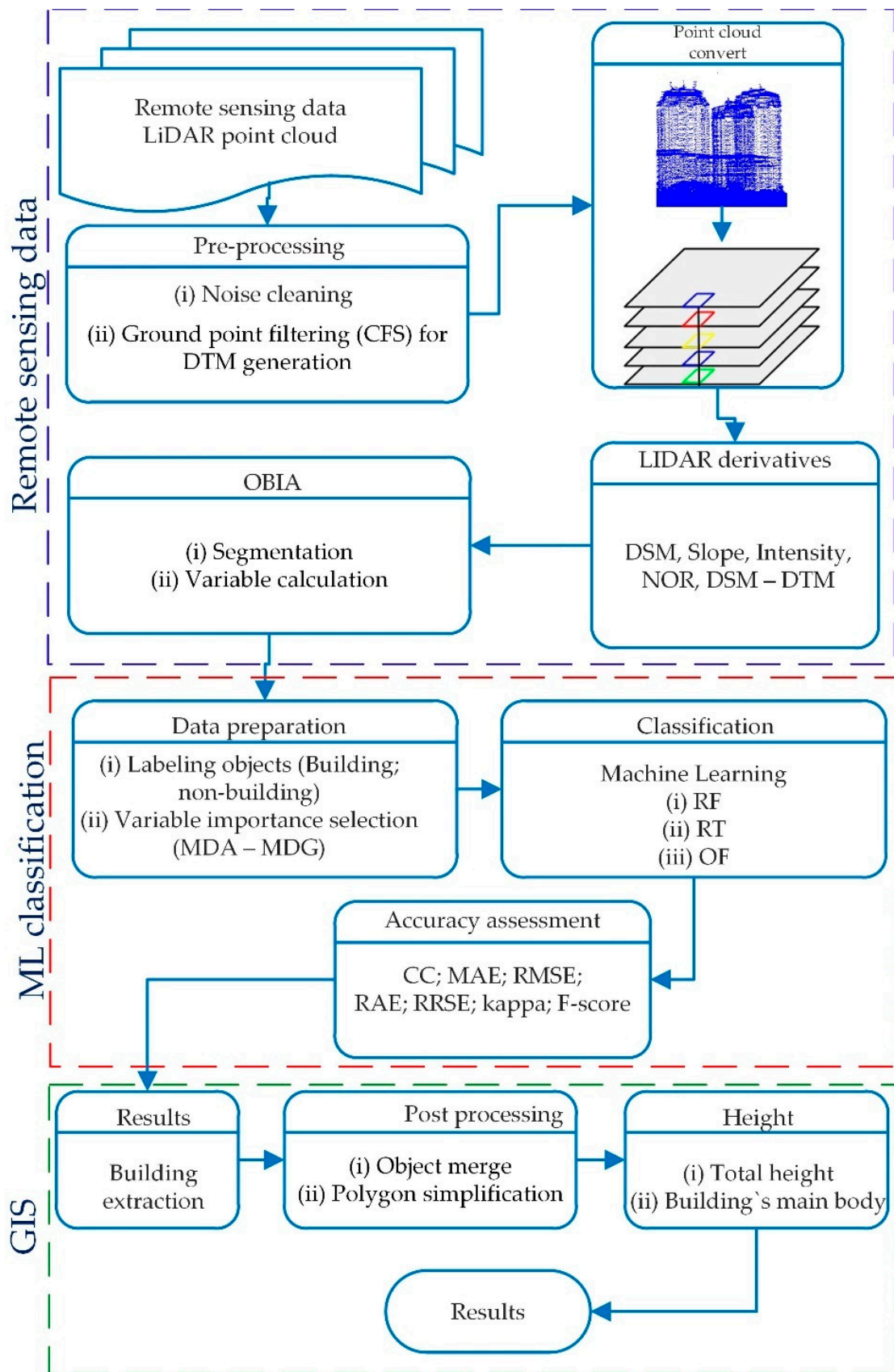
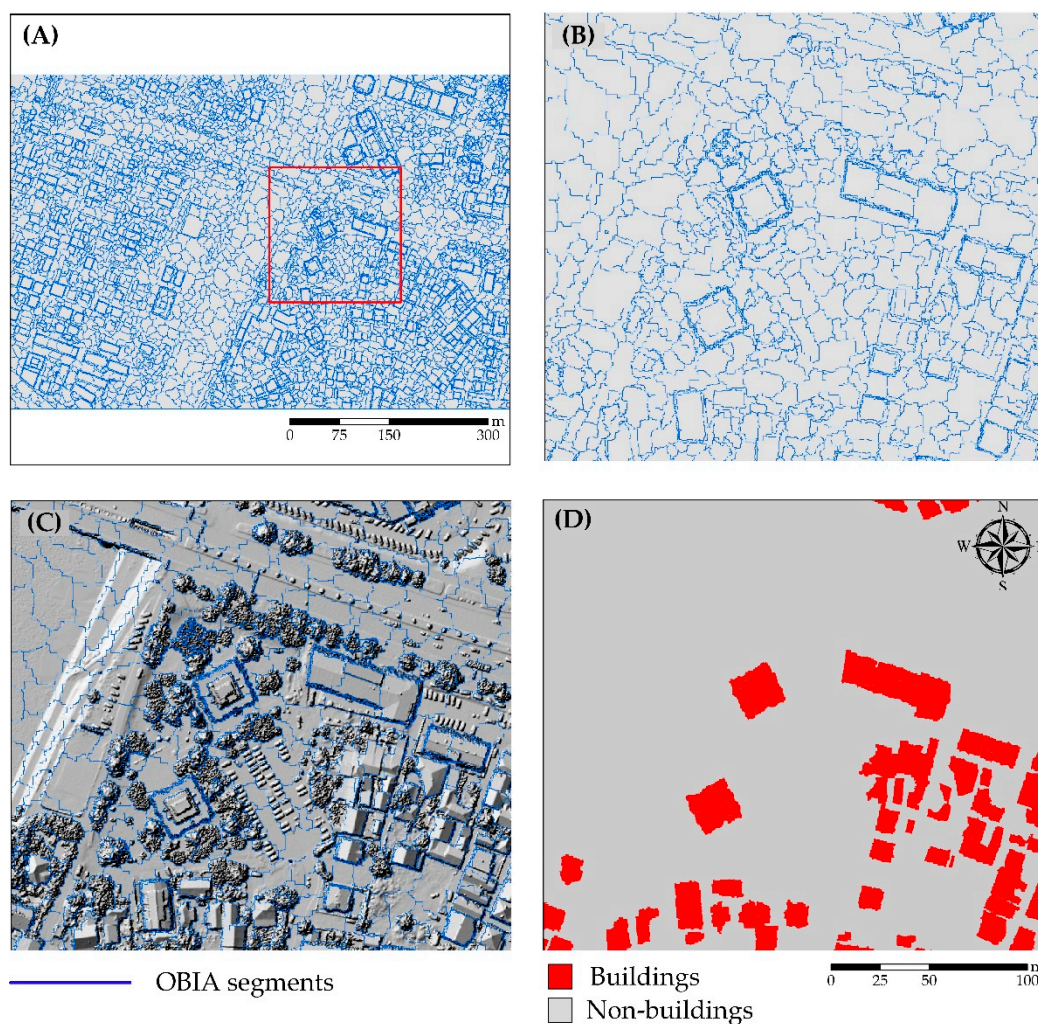


Figure 4. Flowchart of the proposed methodology.

Table 1. Selected variables for building extraction.

Type	Variables
Layers	Mean values of; intensity, slope, DSM, DSM–DTM difference, number of returns. Standard deviation of; intensity, slope, DSM, DSM–DTM difference, number of return.
Geometric	Length/width, asymmetry, compactness, density, elliptic fit, rectangular fit, roundness.
Textural	GLCM homogeneity of slope (GHom_slope), GLCM homogeneity of DSM (GHom_DSM), GLCM dissimilarity of slope (GDis_slope), GLCM dissimilarity of DSM (GDis_DSM), GLCM entropy of slope (GEnt_slope), GLCM entropy of DSM (GEnt_DSM), GLCM angular 2nd moment of slope (GAng2_slope), GLCM angular 2nd moment of DSM (GAng2_DSM).

**Figure 5.** OBIA segmentation and training; (A) segmentation over whole study area; (B) segmentation detail; (C) segmentation detail over hillshade; and (D) training data, detail.

Two different approaches were followed in classifying the datasets with the machine learning algorithms. First, the buildings were extracted using the variables given in Table 1 for two randomly divided datasets. Then, ML algorithms were applied to the datasets using the ten most important variables according to the variable importance calculated with a Mean Decrease in Accuracy (MDA) and Mean Decrease in Gini (MDG), respectively, which are the variable importance measures of the random forest algorithm. The MDA index permits the use of out-of-bag (OOB) observation samples not used in the tree development to calculate the variable importance. It considers the difference between the OOB error

due to a test dataset generated by random permutations of different variable values and the OOB error calculated from the original dataset. The most crucial variable in the MDA index is the one that reduces accuracy the most when it is removed from the dataset. MDG measure is a measure of how each variable used in the classification contributes to the homogeneity in the nodes and leaves in the random forest generated by the training data. If the variable is important, it tends to split mixed-class nodes into pure single-class nodes. The variable with a high MDG value is of high importance.

2.3.2. Machine Learning Classification and Accuracy Assessment

The resolved data were further used for statistical analysis and prediction in Weka; a multi-purpose software developed to apply machine learning algorithms. Random Forest (RF), Random Tree (RT), and Optimized Forest (OF) have been evaluated for the building classification. The segments from the OBIA have been trained from two classes, buildings and non-buildings (Figure 5D).

RT is a supervised classifier that generates a random data collection for building a decision tree. The optimum split across all the variables in the tree is used to divide each node. Random trees are groups of tree predictors [41]. On the other hand, the RF classifier delivers reliable classifications by leveraging predictions generated by an ensemble of decision trees [42]. As RF and RT can have many nodes that often are not very useful in increasing the ensemble accuracy of the forest, Adnan et al. [43], proposed a technique for selecting a small subforest. They proposed OF using genetic algorithms for selecting optimal/near-optimal subforests. These three modelling strategies were chosen for their simplicity and ability to use the model with various data. The models utilized were tested using several accuracy evaluation metrics.

Mean Absolute Error (MAE), an error-based comparison between predicted and observed values, was utilized to measure the model's performance during model processing [44], and Relative Absolute Error (RAE) has been used to measure the performance of the predictive model's REF [45],

$$\text{MAE} = \frac{\sum_{i=1}^n |O_i - P_i|}{n} \quad (1)$$

$$\text{RMAE} = \sqrt{\frac{\sum_{i=1}^n |O_i - P_i|}{n}} \quad (2)$$

where, O_i is the observed and P_i is the predicted value.

In addition, for the accuracy analyses, the standard evaluation statistics for binary classification were used. Namely, true positive (TP) (a class correctly identified), false positive (FP) (a class incorrectly identified; a commission error), and false negative (FN) (a class is missed; an omission error) parameters were taken into consideration. TP, FN, and FP indicate perfect identification, under-identification, and over-identification, respectively. Then the precision (P), recall (R), and F-score (F) were calculated. Precision (i.e., positive predictive value) describes the correctness of extracted buildings and how well the algorithm dealt with FP (Equation (3)), while recall (i.e., sensitivity) describes the building detection rate and how well the algorithm dealt with FN (Equation (4)). The F-score is the harmonic mean of recall and precision and reports the overall accuracy considering both commission and omission errors (Equation (5)). From the confusion matrix, kappa statistics were also calculated [46]. The receiver operating characteristic (ROC) and the precision–recall curve (PRC) were applied against the investigated models to check their precision for building classification. ROC and PRC are designed to assess the performance of the analytical model [47]. Thus, the areas under the curves can be used to estimate the model's overall accuracy. The ideal value for the ROC and PRC values is 1.

$$P = \text{TP} / (\text{TP} + \text{FP}) \quad (3)$$

$$R = \text{TP} / (\text{TP} + \text{FN}) \quad (4)$$

$$F\text{-score} = 2 \times ((P \times R)/(P + R)) \quad (5)$$

For training and testing the model, the data was separated in two ways, 70%–30% and 30%–70%. A total of 5380 segments were produced in the segmentation. Thus, in the 70%–30% data splits, 3766 objects were used for training and 1614 object for testing. The accuracy was evaluated using independent objects that were not part of the training sets.

2.3.3. Post-Processing

Since many building footprints were obtained as more than one object in the segmentation stage, the object patches of the building footprint obtained as a result of the classification stage were merged. After the building extraction stage, we used polygon simplification to represent the building footprint better. Thus, we have used the point remove simplification algorithm, and considering the spatial resolution of the data, we have applied a simplification tolerance of 50 cm. After simplifying the polygons, we have compared the extracted and the actual footprint areas. As a reference to the actual footprint area, the estimated areas were compared with the manually extracted areas over the hillsides of the point cloud.

2.3.4. Building Heights and Footprint Area

The building heights were obtained from the DSM–DTM difference. The extracted building polygons from the OBIA include the building roof area. Here, we extract the average building heights from the DSM–DTM difference. To estimate the roof height, we extract the maximum height value in every building represented by the objects. This way, we try to obtain both heights from the main body of the building and the total height of the building. In addition, we have extracted building heights for the building's body by converting the polygons to lines. Afterwards, the points objects were created for the vertexes of the lines, where height values were extracted from the DSM–DTM differences. A visual representation over a profile from the used point cloud is given in Figure 6. The accuracy assessment of the obtained results was done by comparing the extracted area and the height of the building with the manually extracted area from the hillshade, and the heights from the LiDAR data. For this purpose, we have extracted profiles over the point cloud, and measured the main body's height and the building's total height.

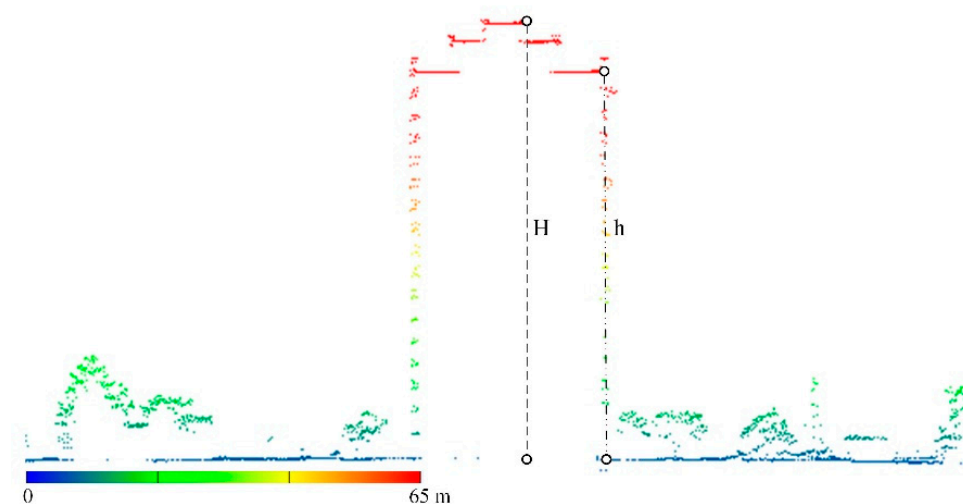


Figure 6. Representation of height from the main body of the building (h); and the total height of the building (H).

3. Results

3.1. Variable Importance

Three different datasets have been used to model each data split. First, we used all 25 variables to classify the buildings. Furthermore, MDA and MDG techniques have been used to select the top 10 variables for both dataset splits. The selected variables are given in Figures 7 and 8 for 70%–30% and 30%–70% training–testing data split, respectively.

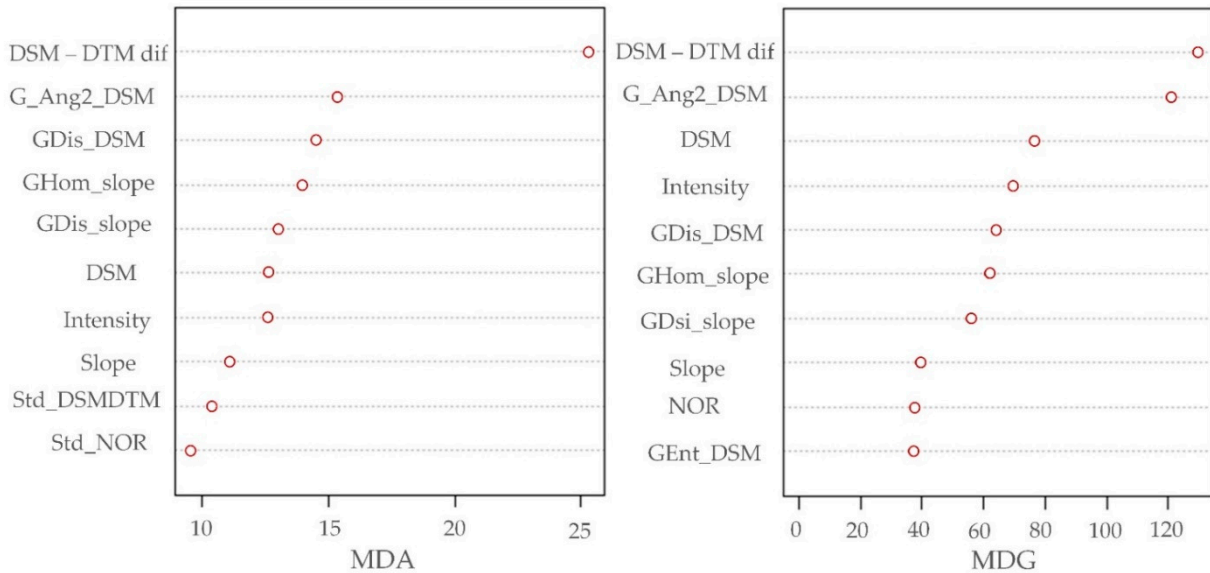


Figure 7. Top 10 variable selection with 70%–30% training–testing data split.

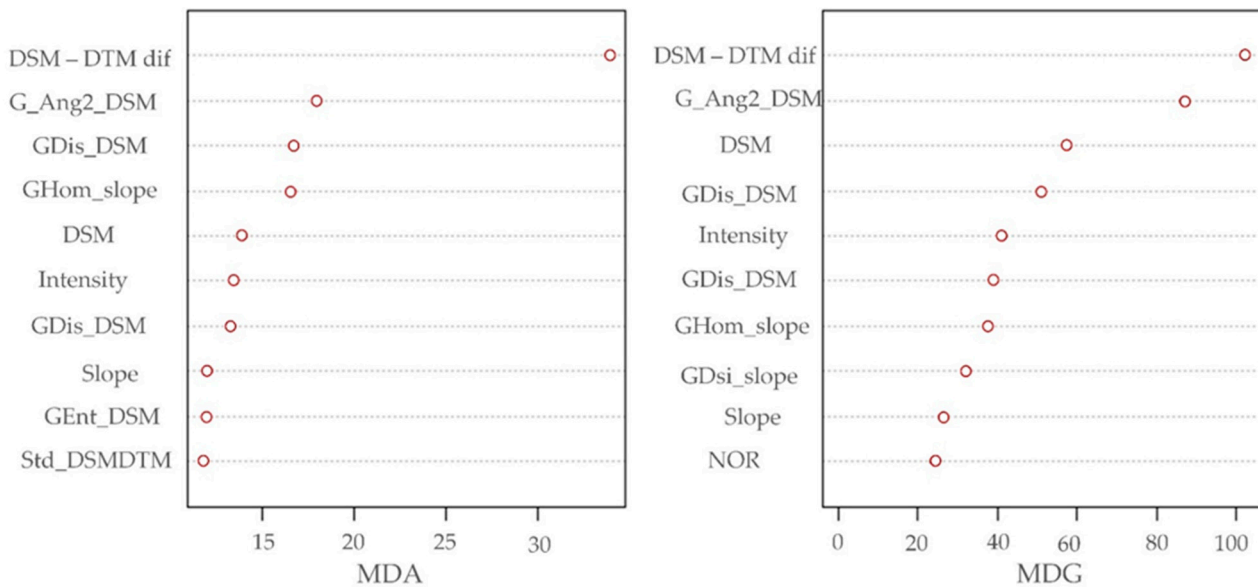


Figure 8. Top 10 variable selection with 30%–70% training–testing data split.

The results show that the difference between DSM and DTM data is the most essential variable in all cases, increasing the MDA by more than 25% in the 70–30 and more than 35% in the 30%–70% data split. The G_Ang2_DSM variable was second, and it can be noticed that its importance was more significant in the MDG variable selection than in the MDA. All of the top variables were Lidar derivatives, and none of the OBIA derivatives concerning the shape of the objects were selected.

3.2. Classification Results

After selecting the top 10 variables using MDA and MDG methods, we have applied three different ML models to classify the object into building and non-building. Thus, we have applied three models to three different datasets and investigated different data splits such as 70–30 and 30–70 for training and testing, respectively. The visual results are presented in Figure 9. From the visual analysis, it can be noticed that buildings were classified with high accuracy. Table 2 presents the accuracy assessment results of the building classification for each ML method, with each variable selection strategy, for both 70% and 30% training and testing data split. RT performed last from the ML methods, while RF and OF showed similar results.

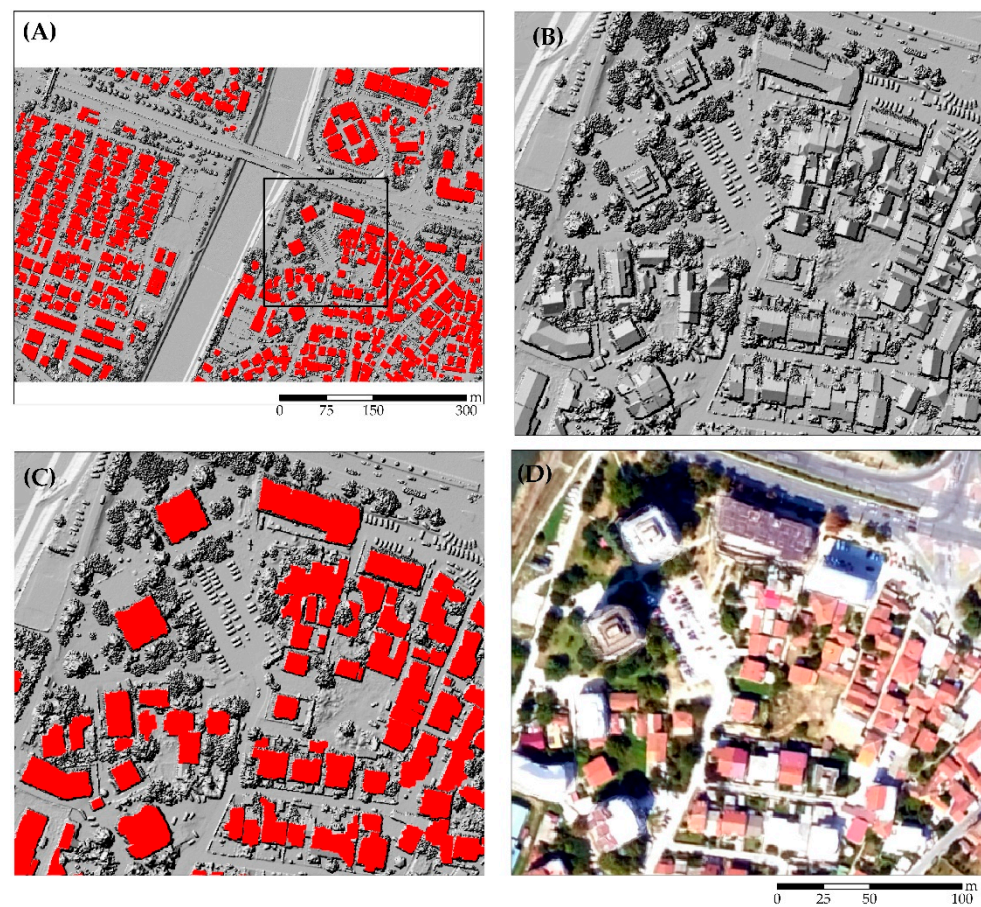


Figure 9. Classification results; (A) building classification over hillshade; (B) hillshade data; (C) detail of building classification over hillshade; and (D) high-resolution orthophoto of the same area.

The accuracy analysis concerning the classification errors shows similar results where the RF and OF results are similar and outperformed RT. As expected, 70% of the training data was more beneficial with slightly lower errors. However, this was not the case for the RF, where with the MDA and MDG variable selection, RT showed lower errors with the more minor training data set. Nevertheless, the errors of RT in all scenarios were significantly higher than the other two ML methods. As for the kappa statistics, the highest values were noticed using the RF, then OF and RT, respectively (Figure 10).

Table 2. Accuracy assessment results of the building classification.

Data Split		Method	CCI	TP Rate	FP Rate	Precision	Recall	F-Score	ROC Area	PRC Area
All variables	70–30	RF	99.0	0.99	0.02	0.98	0.99	0.98	0.99	1.00
		RT	97.7	0.96	0.04	0.95	0.96	0.95	0.95	0.92
		OF	99.1	0.96	0.02	0.99	0.96	0.98	1.00	1.00
	30–70	RF	98.8	0.97	0.03	0.98	0.97	0.97	1.00	1.00
		RT	97.4	0.95	0.06	0.95	0.95	0.94	0.94	0.91
		OF	98.8	0.97	0.03	0.98	0.97	0.97	1.00	1.00
MDA	70–30	RF	98.9	0.99	0.02	0.97	0.98	0.96	0.99	1.00
		RT	98.0	0.96	0.04	0.96	0.96	0.96	0.96	0.93
		OF	99.1	0.99	0.02	0.98	0.99	0.98	1.00	1.00
	30–70	RF	98.6	0.97	0.04	0.98	0.97	0.97	1.00	1.00
		RT	98.1	0.96	0.04	0.96	0.96	0.96	0.96	0.93
		OF	98.6	0.97	0.04	0.98	0.97	0.97	1.00	1.00
MDG	70–30	RF	98.9	0.98	0.03	0.97	0.98	0.98	1.00	1.00
		RT	97.8	0.96	0.04	0.95	0.96	0.96	0.96	0.92
		OF	99.1	0.98	0.03	0.97	0.97	0.98	1.00	0.99
	30–70	RF	98.6	0.97	0.04	0.97	0.97	0.97	1.00	1.00
		RT	98.1	0.96	0.05	0.96	0.96	0.96	0.96	0.93
		OF	98.7	0.98	0.03	0.98	0.97	0.97	1.00	1.00

70–30 refers to 70% training, and 30% of testing data have been used for modelling. Same for 30–70. CCI is Correctly Classified Instances.

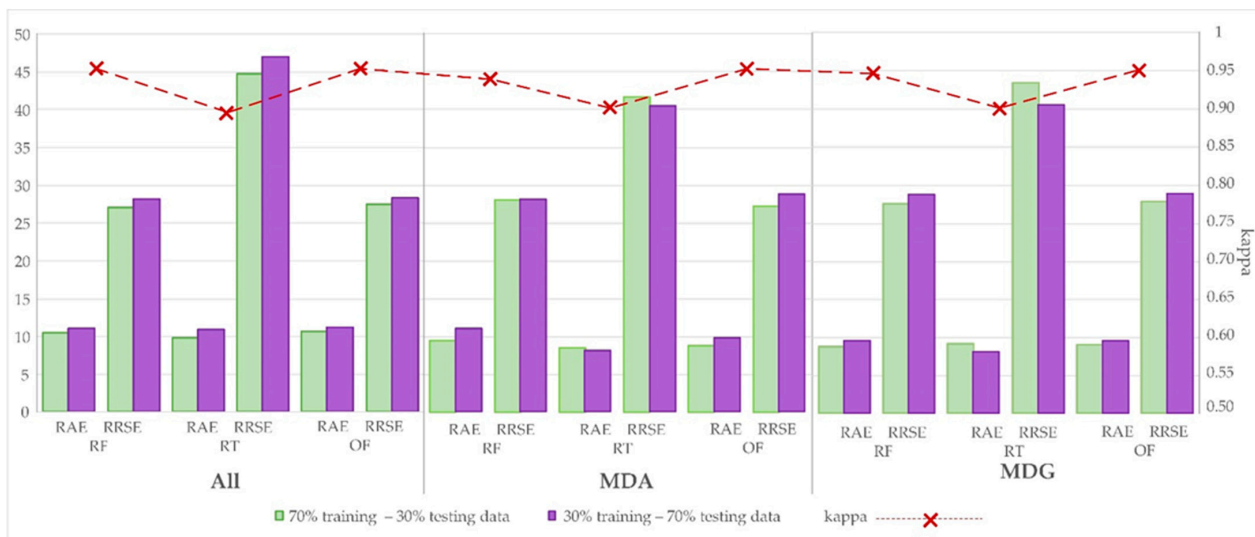


Figure 10. Accuracy assessment of the used modeling methods and variable selecting strategy.

3.3. Building Heights and Footprint Area

With a visual analysis, it has been concluded that the polygons can be simplified without losing any essential data with a simplification tolerance of 50 cm. The results are given in Figure 11, where the blue lines represent the simplified building segments. It can be seen that the simplified segments better represent the roof of the buildings. Afterwards, we compared the simplified buildings' area with the manually calculated area of the buildings over the hilshade data where the rooftops can be seen. The comparison of the results and the actual areas showed that the methodology tend to estimate the area approximately 6% smaller than the actual footprint of the building. Additionally, the RMSE is 30.4 m².

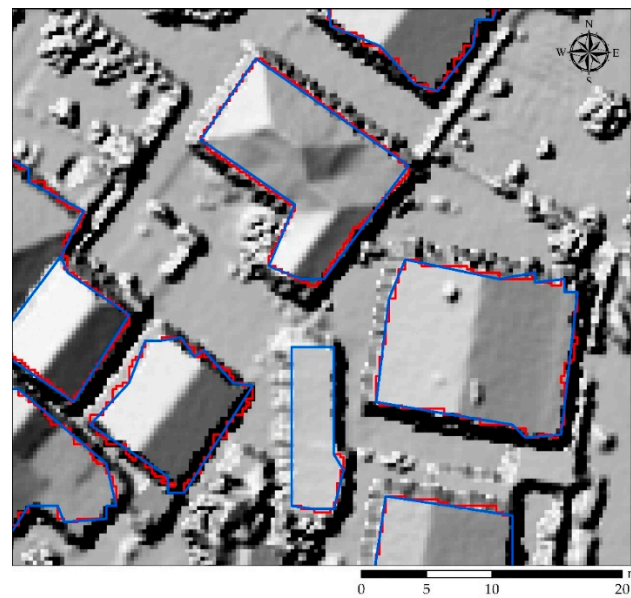


Figure 11. Post-processing results; red line original segments; and blue line simplified segments.

Two different building height data have been extracted, from the top of the building and the main body of the building. For the top of the building, we used the maximum pixel value of the DSM–DTM difference. For the building’s main body, we have used mean pixel values and DSM–DTM difference at the vertexes of the building’s polygons. The results showed that the mean percentage difference between the actual maximum and the estimated height of the buildings is 0.8%, with a maximum difference of 4.3% and a minimum difference of -0.01% . The RMSE was 0.25 m.

For the body of the main building, the percentile difference between the actual and predicted heights using the mean pixel values was 7%, and RMSE 1.47 m, while using the mean vertex values, a 2.5% difference was obtained, with an RMSE of 1.17 m. With the use of the mean vertex value, we were able to obtain results with better accuracy. Compared with the mean pixel value method, the first one tends to estimate the buildings’ heights as lower than the actual values (Figure 12).

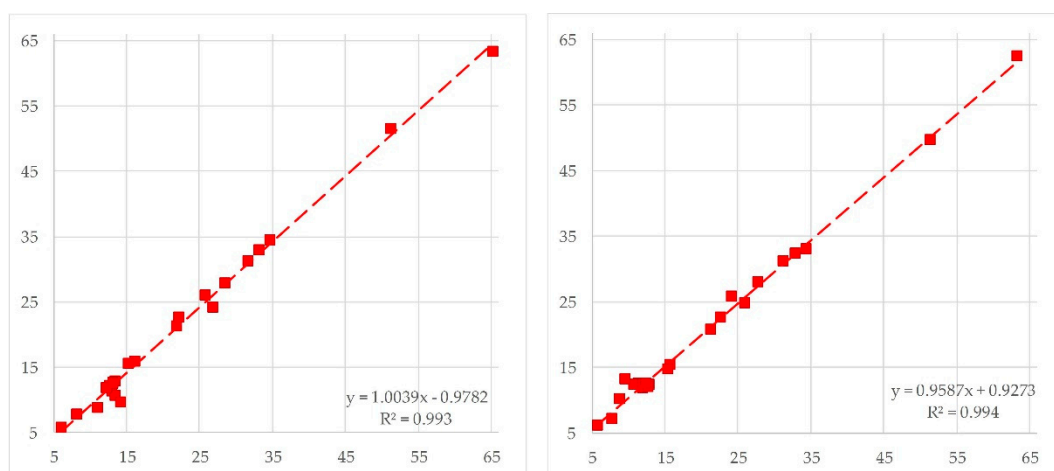


Figure 12. Correlation between actual and estimated buildings’ heights from; left—mean pixel values; right—mean vertex values.

4. Discussion

The study demonstrates a building inventory information extraction from remote sensing data extracted from LiDAR data. The results show that specific building information such as footprint area, total height, and height of the building's main body can be extracted from the investigated data with high accuracy. This was achieved with the use of ML algorithms and careful variable selection. In the variable selection stage, the DSM–DTM difference variable was obtained as the most crucial parameter in all data sets. This is because the study area has a flat topography, so the height difference between buildings and ground and small objects is distinctive for classification. It has been noticed that intensity, DSM, slope, and DSM–DTM difference layers used as input in the study are among the ten most essential parameters in all data sets. It has been observed that these layers, produced as LiDAR derivatives, are essential variables for building extraction. It has been seen in the variable importance analysis that the effect of the textural variables produced from DSM and slope data on the building extraction is high. In particular, the variable G-Ang2_DSM was determined as the second most crucial variable in all data sets. Textural variables were essential in distinguishing buildings and trees from each other, while these features are more regular in buildings, but more irregular in trees.

The investigated ML algorithms have been frequently used for different applications in the last few years [48]. While all the investigated algorithms showed good performance, the results show that RF and OF outperformed RT, which produced the highest errors and the lowest kappa values resulting from the building classification. RF and OF showed relatively similar results, with negligible differences. Considering the two investigated data splits in this study, we can conclude that the methodology used can give good results even with a small dataset. For instance, in the 70% training and 30% testing dataset, the OF resulted in 99.1% CCI, while in the 30%–70%, 98.8%. Similar, the F-score for RF and OF with 70% training was 0.98, while with 30%, 0.97.

The building height was defined in two different ways in this study. The first is the entire building height from the ground level to the peak point of the roof, which is mentioned as the roof height (H). The second one is the height from the ground to the tip of the roof cover, which is mentioned as the main body height (h) (Figure 6). The latter height is more meaningful in structural engineering since it represents the height of the last slab from the ground level. The building roof and the main body heights have been automatically calculated for building heights. The maximum height falling into the building polygons was obtained automatically from the DSM–DTM difference layer for the roof height. When the H values are compared with the manually obtained height values, it is seen that the RMSE value is 0.25 m. This result shows that the applied method can obtain the building roof heights with high accuracy. Two different approaches were used to extract the heights of the main body of the building. The first is the average height value falling inside the building footprint polygon. The other one is the average height value below the vertex points of the building polygon. When the h values obtained by both methods were compared with the manually obtained height values, the RMSE values for mean height and vertex height were obtained as 1.47 m and 1.17 m, respectively. Thus, it can be concluded that the results obtained with the vertex height have higher accuracy than the mean height. On the other hand, it is seen that the main body height values are obtained with lower accuracy compared to the roof height. In the building extraction method applied in the study, the polygons belonging to the footprints of the building boundaries are extracted. This margin of error is an expected result, as the average of all heights within the polygon is calculated in the height values calculated according to the mean height. Since the buildings in the study area have different roof types, such as flat, gabled, hipped, and pyramidal, these differences may arise from the average vertex height values.

In the rapid structural safety assessment applications using remote sensing data, the second step after extracting the building height is estimating the fundamental vibration period of the buildings. For this estimation, the empirical equations that predict the building period concerning the building height are usually used [49]. To understand whether the

extracted building heights in this study are accurate enough to use in the rapid seismic safety assessment or not, the following approach might be applied; the RMSE values calculated in this study are 0.25 m for roof height, and 1.47 m and 1.17 m for the main body height; if these numbers are put into one of the building period estimation equations, for example, $T = 0.0195H$ [7], it would be seen that the effect of these RMSE values on the building period will be very limited to the 0.005s for the roof height, and 0.03 and 0.02s for the main body height. Since these period differences are minimal and their effect on the earthquake force calculations is negligible, the accuracy of the results of this study can be considered reasonable concerning the nature of rapid structural safety assessment using remote sensing data.

Moreover, the building area estimation is a valuable parameter for building inventory databases, which can be used to estimate the floor masses and, if the number of floors is also known, the entire mass of the buildings. Since the earthquake force acting on a building is a function of the total mass, it is a crucial parameter for seismic safety assessments on the urban scale.

It is beyond the scope of this study to estimate the year of building construction. As mentioned in the introduction, the construction year is also a crucial parameter in structural health monitoring. For this, additional data are required since the dataset used in the presented study has been collected on a single date. Previous studies have used high-resolution optical satellite imagery from two different years [49]. Thus, future studies should consider the buildings' construction year and other relevant information.

5. Conclusions

Many data types may be used to gather an inventory of buildings based on remote sensing. Critical risk assessment building elements such as the year of construction, building height, and building size may be determined. This study's primary goals were established to provide structural engineers with the information they need to do the necessary calculations for the seismic performance of existing structures. Thus, we used LiDAR derivatives for building classification using machine learning algorithms and estimate crucial information, such as footprint area and different heights of the buildings, such as the height of the main body and rooftop. Although this study has several investigated objectives, the most important conclusion is that LiDAR derivatives data can be used for sensitive building inventory information extraction. The results of the study are promising in terms of various data extraction from a single dataset. As in some applications, the time for action is limited, and a rapid extraction of building inventory is crucial. The key point is that accurate results can be produced with a small amount of training data, which is beneficial in terms of time. The results can be used in many applications, but most importantly, in structural safety assessment. To complete the necessary data for such applications, the year of construction of the building is required, and it is in sight for future studies. For future studies, the shape as well as the material of the building can also be considered.

Author Contributions: Conceptualization, Resul Comert, Gordana Kaplan, Onur Kaplan, Ugur Avdan and Dilek Kucuk Matci; methodology, Resul Comert, Gordana Kaplan and Onur Kaplan; software, Resul Comert and Gordana Kaplan; validation, Gordana Kaplan and Ugur Avdan; formal analysis, Gordana Kaplan; writing—original draft preparation, Gordana Kaplan; writing—review and editing, Gordana Kaplan, Dilek Kucuk Matci, Resul Comert, Onur Kaplan and Ugur Avdan; visualization, Gordana Kaplan. All authors have read and agreed to the published version of the manuscript.

Funding: This research received no external funding.

Data Availability Statement: Not applicable.

Acknowledgments: The authors acknowledge using Lidar data provided by the Cadaster Agency of North Macedonia as test data from katastar.gov.mk, accessed on 31 August 2022.

Conflicts of Interest: The authors declare no conflict of interest.

References

1. Kaplan, O.; Guney, Y.; Topcu, A.; Ozcelikors, Y. A rapid seismic safety assessment method for mid-rise reinforced concrete buildings. *Bull. Earthq. Eng.* **2018**, *16*, 889–915. [\[CrossRef\]](#)
2. Crowley, H.; Pinho, R. Period-height relationship for existing European reinforced concrete buildings. *J. Earthq. Eng.* **2004**, *8*, 93–119. [\[CrossRef\]](#)
3. Goel, R.K.; Chopra, A.K. Period formulas for moment-resisting frame buildings. *J. Struct. Eng.* **1997**, *123*, 1454–1461. [\[CrossRef\]](#)
4. Masi, A.; Vona, M. *Estimation of the Period of Vibration of Existing RC Building Types Based on Experimental Data and Numerical Results*; Springer: Dordrecht, The Netherlands, 2009.
5. Pan, T.-C.; Goh, K.S.; Megawati, K. Empirical relationships between natural vibration period and height of buildings in Singapore. *Earthq. Eng. Struct. Dyn.* **2014**, *43*, 449–465. [\[CrossRef\]](#)
6. Hong, L.-L.; Hwang, W.-L. Empirical formula for fundamental vibration periods of reinforced concrete buildings in Taiwan. *Earthq. Eng. Struct. Dyn.* **2000**, *29*, 327–337. [\[CrossRef\]](#)
7. Kaplan, O.; Guney, Y.; Dogangun, A. A period-height relationship for newly constructed mid-rise reinforced concrete buildings in Turkey. *Eng. Struct.* **2021**, *232*, 111807. [\[CrossRef\]](#)
8. Hu, Q.; Zhen, L.; Mao, Y.; Zhou, X.; Zhou, G. Automated building extraction using satellite remote sensing imagery. *Autom. Constr.* **2021**, *123*, 103509. [\[CrossRef\]](#)
9. Kim, T.; Javzandulam, T.; Lee, T.-Y. Semiautomatic reconstruction of building height and footprints from single satellite images. In Proceedings of the 2007 IEEE International Geoscience and Remote Sensing Symposium, Barcelona, Spain, 23–28 July 2007; IEEE: New York, NY, USA, 2007.
10. Awrangjeb, M.; Hu, X.; Yang, B.; Tian, J. Editorial for Special Issue: “Remote Sensing based Building Extraction”. *Remote Sens.* **2020**, *12*, 549. [\[CrossRef\]](#)
11. Schlosser, A.; Szabó, G.; Bertalan, L.; Varga, Z.; Enyedi, P.; Szabó, S. Building extraction using orthophotos and dense point cloud derived from visual band aerial imagery based on machine learning and segmentation. *Remote Sens.* **2020**, *12*, 2397. [\[CrossRef\]](#)
12. Turker, M.; Koc-San, D. Building extraction from high-resolution optical spaceborne images using the integration of support vector machine (SVM) classification, Hough transformation and perceptual grouping. *Int. J. Appl. Earth Obs. Geoinf.* **2015**, *34*, 58–69. [\[CrossRef\]](#)
13. Huang, X.; Zhang, L. Morphological building/shadow index for building extraction from high-resolution imagery over urban areas. *IEEE J. Sel. Top. Appl. Earth Obs. Remote Sens.* **2011**, *5*, 161–172. [\[CrossRef\]](#)
14. Nebiker, S.; Lack, N.; Deuber, M. Building change detection from historical aerial photographs using dense image matching and object-based image analysis. *Remote Sens.* **2014**, *6*, 8310–8336. [\[CrossRef\]](#)
15. Xie, Y.; Feng, D.; Xiong, S.; Zhu, J.; Liu, Y. Multi-scene building height estimation method based on shadow in high resolution imagery. *Remote Sens.* **2021**, *13*, 2862. [\[CrossRef\]](#)
16. Zhang, C.; Cui, Y.; Zhu, Z.; Jiang, S.; Jiang, W. Building Height Extraction from GF-7 Satellite Images Based on Roof Contour Constrained Stereo Matching. *Remote Sens.* **2022**, *14*, 1566. [\[CrossRef\]](#)
17. Panagiotakis, E.; Chrysoulakis, N.; Charalampopoulou, V.; Poursanidis, D. Validation of Pleiades Tri-Stereo DSM in urban areas. *ISPRS Int. J. Geo-Inf.* **2018**, *7*, 118. [\[CrossRef\]](#)
18. Maltezos, E.; Ioannidis, C. Automatic Extraction of Building Roof Planes from Airborne Lidar Data Applying an Extended 3D Randomized Hough Transform. *ISPRS Ann. Photogramm. Remote Sens. Spat. Inf. Sci.* **2016**, *3*, 209–216. [\[CrossRef\]](#)
19. Yi, Z.; Wang, H.; Duan, G.; Wang, Z. An airborne LiDAR building-extraction method based on the naive Bayes–RANSAC method for proportional segmentation of quantitative features. *J. Indian Soc. Remote Sens.* **2021**, *49*, 393–404. [\[CrossRef\]](#)
20. Tolt, G.; Persson, Å.; Landgård, J.; Söderman, U. Segmentation and classification of airborne laser scanner data for ground and building detection. In Proceedings of the Laser Radar Technology and Applications XI, Orlando, FL, USA, 19 May 2006; International Society for Optics and Photonics: San Diego, CA, USA, 2006.
21. Awrangjeb, M.; Fraser, C.S. Rule-based segmentation of LIDAR point cloud for automatic extraction of building roof planes. *ISPRS Ann. Photogramm. Remote Sens. Spat. Inf. Sci.* **2013**, *2*, 1–6. [\[CrossRef\]](#)
22. Yang, B.; Wei, Z.; Li, Q.; Li, J. Semiautomated building facade footprint extraction from mobile LiDAR point clouds. *IEEE Geosci. Remote Sens. Lett.* **2012**, *10*, 766–770. [\[CrossRef\]](#)
23. Albano, R. Investigation on roof segmentation for 3D building reconstruction from aerial LIDAR point clouds. *Appl. Sci.* **2019**, *9*, 4674. [\[CrossRef\]](#)
24. Forlani, G.; Nardinocchi, C.; Scaioni, M.; Zingaretti, P. Complete classification of raw LIDAR data and 3D reconstruction of buildings. *Pattern Anal. Appl.* **2006**, *8*, 357–374. [\[CrossRef\]](#)
25. Wang, J.; Shan, J. Segmentation of LiDAR point clouds for building extraction in American Society for Photogramm. In Proceedings of the Remote Sensing Annual Conference, Baltimore, MD, USA, 9–13 March 2009.
26. Awrangjeb, M.; Lu, G.; Fraser, C. Automatic Building Extraction from Lidar Data Covering Complex Urban Scenes. *Int. Arch. Photogramm. Remote Sens. Spat. Inf. Sci.* **2014**, *XL-3*, 25–32. [\[CrossRef\]](#)
27. Sohn, G.; Dowman, I. Data fusion of high-resolution satellite imagery and LiDAR data for automatic building extraction. *ISPRS J. Photogramm. Remote Sens.* **2007**, *62*, 43–63. [\[CrossRef\]](#)
28. Wang, X.; Li, P. Extraction of urban building damage using spectral, height and corner information from VHR satellite images and airborne LiDAR data. *ISPRS J. Photogramm. Remote Sens.* **2020**, *159*, 322–336. [\[CrossRef\]](#)

29. O'Neil-Dunne, J.P.; MacFaden, S.W.; Royar, A.R.; Pelletier, K.C. An object-based system for LiDAR data fusion and feature extraction. *Geocarto Int.* **2013**, *28*, 227–242. [[CrossRef](#)]
30. Zarro, C.; Ullo, S.; Meoli, G.; Focareta, M. Semi-automatic classification of building from low-density Lidar data and worldview-2 images through OBIA technique. In Proceedings of the IGARSS 2020 IEEE International Geoscience and Remote Sensing Symposium, Waikoloa, HI, USA, 26 September–2 October 2020; IEEE: New York, NY, USA, 2020.
31. Cal, A. *High-Resolution Object-Based Building Extraction Using PCA of LiDAR nDSM and Aerial Photos, in Spatial Variability in Environmental Science-Patterns, Processes, and Analyses*; IntechOpen: Rijeka, Croatia, 2020.
32. Gilani, S.A.N.; Awrangjeb, M.; Lu, G. An automatic building extraction and regularisation technique using lidar point cloud data and orthoimage. *Remote Sens.* **2016**, *8*, 258. [[CrossRef](#)]
33. Guo, L.; Deng, X.; Liu, Y.; He, H.; Lin, H.; Qiu, G.; Yang, W. Extraction of dense urban buildings from photogrammetric and LiDAR point clouds. *IEEE Access* **2021**, *9*, 111823–111832. [[CrossRef](#)]
34. Tomljenovic, I.; Tiede, D.; Blaschke, T. A building extraction approach for Airborne Laser Scanner data utilizing the Object Based Image Analysis paradigm. *Int. J. Appl. Earth Obs. Geoinf.* **2016**, *52*, 137–148. [[CrossRef](#)]
35. Belgiu, M.; Tomljenovic, I.; Lampoltshammer, T.J.; Blaschke, T.; Höfle, B. Ontology-based classification of building types detected from airborne laser scanning data. *Remote Sens.* **2014**, *6*, 1347–1366. [[CrossRef](#)]
36. Sinadinovski, C.; Markušić, S.; Stanko, D.; McCue, K.F.; Pekevski, L. Seismic Analysis of Moderate Size Earthquakes Recorded on Stations at Close Epicentral Distances. *Appl. Sci.* **2022**, *12*, 470. [[CrossRef](#)]
37. Zhang, W.; Qi, J.; Wan, P.; Wang, H.; Xie, D.; Wang, X.; Yan, G. An easy-to-use airborne LiDAR data filtering method based on cloth simulation. *Remote Sens.* **2016**, *8*, 501. [[CrossRef](#)]
38. Benz, U.C.; Hofmann, P.; Willhauck, G.; Lingenfelder, I.; Heynen, M. Multi-resolution, object-oriented fuzzy analysis of remote sensing data for GIS-ready information. *ISPRS J. Photogramm. Remote Sens.* **2004**, *58*, 239–258. [[CrossRef](#)]
39. Comert, R. Investigation of the effect of the dataset size and type in the earthquake-triggered landslides mapping: A case study for the 2018 Hokkaido Iburu landslides. *Front. Earth Sci.* **2021**, *9*, 23. [[CrossRef](#)]
40. Shirvani, Z.; Abdi, O.; Buchroithner, M. A synergetic analysis of Sentinel-1 and-2 for mapping historical landslides using object-oriented Random Forest in the Hyrcanian forests. *Remote Sens.* **2019**, *11*, 2300. [[CrossRef](#)]
41. Kiranmai, S.A.; Laxmi, A.J. Data mining for classification of power quality problems using WEKA and the effect of attributes on classification accuracy. *Prot. Control. Mod. Power Syst.* **2018**, *3*, 1–12. [[CrossRef](#)]
42. Belgiu, M.; Drăguț, L. Random forest in remote sensing: A review of applications and future directions. *ISPRS J. Photogramm. Remote Sens.* **2016**, *114*, 24–31. [[CrossRef](#)]
43. Adnan, M.N.; Islam, M.Z. Optimizing the number of trees in a decision forest to discover a subforest with high ensemble accuracy using a genetic algorithm. *Knowl.-Based Syst.* **2016**, *110*, 86–97. [[CrossRef](#)]
44. Pham, B.T.; Jaafari, A.; Nguyen-Thoi, T.; Van Phong, T.; Nguyen, H.D.; Satyam, N.; Masroor, M.; Rehman, S.; Sajjad, H.; Sahana, M.; et al. Ensemble machine learning models based on Reduced Error Pruning Tree for prediction of rainfall-induced landslides. *Int. J. Digit. Earth* **2021**, *14*, 575–596. [[CrossRef](#)]
45. Moayedi, H.; Jamali, A.; Gibril, M.B.A.; Foong, L.K.; Bahiraei, M. Evaluation of tree-base data mining algorithms in land used/land cover mapping in a semi-arid environment through Landsat 8 OLI image; Shiraz, Iran. *Geomat. Nat. Hazards Risk* **2020**, *11*, 724–741. [[CrossRef](#)]
46. Kaplan, O.; Kaplan, G. Response spectra-based post-earthquake rapid structural damage estimation approach aided with remote sensing data: 2020 Samos Earthquake. *Buildings* **2021**, *12*, 14. [[CrossRef](#)]
47. Naderpour, M.; Rizeei, H.; Ramezani, F. Forest fire risk prediction: A spatial deep neural network-based framework. *Remote Sens.* **2021**, *13*, 2513. [[CrossRef](#)]
48. Kaplan, G.; Aydinli, H.O.; Pietrelli, A.; Mieleveville, F.; Ferrara, V. Oil-Contaminated Soil Modeling and Remediation Monitoring in Arid Areas Using Remote Sensing. *Remote Sens.* **2022**, *14*, 2500. [[CrossRef](#)]
49. Kaplan, G.; Kaplan, O. PlanetScope Imagery for Extracting Building Inventory Information. *Environ. Sci. Proc.* **2020**, *5*, 19.